Brittle and Elastic Ice Shelves, Part 1: Wave Propagation

Bradley Paul Lipovsky

[1]Department of Earth and Planetary Sciences, Harvard University

Key Points:

- I describe wave propagation on a buoyantly floating, elastic ice shelf above a uniform and inviscid ocean.
- At wavelength much greater than the ice thickness, waves are either dispersive flexural-gravity waves or nondispersive extensional waves.
- I calculate dispersive wave impedances to infer peak wave-induced stresses of 2.3 kPa near the Nascent Iceberg on the Ross Ice Shelf.

Corresponding author: Bradley Paul Lipovsky, brad_lipovsky@fas.harvard.edu

Abstract

Seismic observations show that distant storms, tsunamis, and earthquakes generate waves on floating ice shelves. In order to quantify the stresses associated with these waves, I describe wave motion an elastic, finite-thickness, buoyantly floating ice layer above a uniform and inviscid water layer. I place particular focus on waves with wavelength greater than the ice thickness, as have recently been observed on the Antarctic ice shelves. I show that long wavelength waves propagate as either extensional or flexural modes. I use this theory to infer the stresses associated with the seismically observed wave field on the Ross Ice Shelf. I find that on the Ross Ice Shelf, flexural gravity waves carry greater stress changes than extensional mode waves, despite the latter having greater particle velocity amplitude. A forthcoming paper explores these stresses in relation to ice shelf rift propagation. This study contributes to our knowledge of the state of stress within floating ice shelves.

1 Introduction

Iceberg calving is fundamental to the dynamics of glaciers and ice sheets that intersect open water [*Bartholomaus et al.*, 2013; *Schoof et al.*, 2017]. Despite this importance, uncertainty in calving physics are currently responsible for large discrepancies in estimates of future sea level rise [*Golledge et al.*, 2015; *DeConto and Pollard*, 2016], and also complicate the interpretation of the paleoclimatological record [*Hulbe et al.*, 2004]. A particular challenge in understanding observed calving behavior is to understand its irregular –and sometimes apparently random– pace [*Fricker et al.*, 2005; *Walker et al.*, 2013; *Banwell et al.*, 2017]. *Benn et al.* [2007] has suggested that this difficulty is due in large part to the difficulty of understanding the state of stress at the calving front during iceberg calving. Because seismometers located on or within glaciers and ice shelves are directly sensitive to the stresses associated with the elastic wave field, seismic observations have tremendous potential to elucidate the mechanics of calving.

The purpose of this paper is to develop a theory of wave propagation in ice shelves. The traditional description of coupled elastic-ocean waves is essentially that of open water surface gravity waves with the free surface replaced by an elastic beam. These waves are called flexural gravity waves; the mechanics of this system were first described by *Greenhill* [1886]. Flexural gravity waves differ from a purely elastic description of the water layer where the fluid has zero elastic shear modulus but does not flow [*Press and Ewing*, 1951]. Recent work has explored flexural gravity wave motion in floating icebergs [*Goodman et al.*, 1980], ice shelves [*Sergienko*, 2010, 2013], and sea ice [*Squire et al.*, 1995].

A hallmark of flexural motions is that the displacement field is dominantly in the vertical direction. Recent observations from the Ross Ice Shelf, however, have shown the existence of long period waves with dominantly horizontal motion [*Bromirski et al.*, 2015, 2017]. Dominantly horizontal wave motion has also been observed in detailed three-dimensional elastic wave simulations using realistic ice shelf geometries [*Sergienko*, 2010; *Konovalov*, 2014; *Sergienko*, 2017]. These waves cannot be explained by flexural gravity wave theory.

In this paper, I derive the general equations of motion for a thin, buoyantly floating elastic solid coupled to an underlying fluid layer (Section 2). The resulting wave behavior is a generalization of the problem of waves trapped thin plate in a vacuum, often called Lamb waves after *Lamb* [1917]. Aspects of this problem have been previously examined by *Wang and Shen* [2010]. The treatment presented differs from that of *Wang and Shen* [2010] in two ways. First, the derivation of the key results is taken using independent analytical methods; and second, the presentation here gives extra attention to aspects of the general theory that are useful for understanding observations from Antarctic Ice Shelves.

I focus attention on the long wavelength limit where wavelengths are greater than the elastic layer thickness. This limit is useful because seismic observations from Antarctic ice shelves show that a large fraction of wave energy occurs in this limit [*Bromirski et al.*, 2010;

Lescarmontier et al., 2012; *Bromirski et al.*, 2017]. I show that long wavelength wave motion consists of two modes. The first mode is the well known flexural-gravity wave mode described above. Motions in this mode are antisymmetric, or flexural, about the mid plane of the elastic layer and wave motion is strongly coupled between the solid ice and the fluid ocean. I show that the second mode is identical to the symmetric mode of the Lamb wave problem. Motions in this mode are symmetric, or extensional, about the mid plane of the elastic layer and wave motion experiences no coupling between the solid ice and the fluid ocean. It is important to emphasize that this decomposition into two modes only occurs in the long wavelength limit. Shorter wavelength motions are more complicated due to mode coupling. Sections 2-4 are necessarily technical in nature and some readers may just be interested in the analysis of seismic data presented in Sections 5. It is worth highlighting that the main result of Sections 2-4 is Equation 53, which provides a Fourier-domain method for calculating stresses from seismograms recorded on or within glaciers and ice shelves.

I analyze seismograms from the Ross Ice Shelf in Section 5. Observed seismograms show extensional waves with greater amplitude than flexural waves by a factor of three. In order to calculate the stress change associated with a given velocity seismogram, I calculate the transfer function between velocity and stress, also called the wave impedance, for both extensional and flexural modes. I find that despite their lower velocity amplitude, the observed flexural waves carry a greater stress change than the observed extensional waves. In a forthcoming companion paper, I relate these stresses to the stresses required to cause rift propagation.

The analysis presented here connects theoretical predictions of ice shelf instability [*Holdsworth and Glynn*, 1978] to geophysical measurement [*MacAyeal et al.*, 2006; *Cathles et al.*, 2009; *Brunt et al.*, 2011] and therefore unleashes the power of seismology to elucidate the detailed mechanics of ice shelf rift propagation.

2 Governing Equations

2.1 The elastic ice layer

I consider a coordinate system with the z direction being positive upwards and x being positive in the direction of ice flow. An ice layer that is initially at rest and everywhere at overburden pressure occupies the region between $z = h$ and $z = -h$. The entire geometry is assumed to be translationally invariant in the x direction, and I take $u_y = \partial/\partial y = 0$ so that deformations are in a state of plane strain. Perturbations to this initial state obey the momentum balance equations,

$$\rho_i \frac{\partial^2 u_x}{\partial t^2} = \frac{\partial \sigma_{xx}}{\partial x} + \frac{\partial \sigma_{xz}}{\partial z}, \tag{1}$$

$$\rho_i \frac{\partial^2 u_z}{\partial t^2} = \frac{\partial \sigma_{xz}}{\partial z} + \frac{\partial \sigma_{zz}}{\partial z}, \tag{2}$$

for ice density ρ_i and stress tensor σ_{ij}. Stresses are related to displacement gradients through the constitutive relationship [*Malvern*, 1969],

$$\sigma_{ij} = \lambda \left(\frac{\partial u_k}{\partial x_k} \right) \delta_{ij} + \mu \left(\frac{\partial u_i}{\partial x_j} + \frac{\partial u_j}{\partial x_i} \right), \tag{3}$$

where, for simplicity, elastic anisotropy is neglected. The values of elastic moduli, here written using Lamé's parameter λ and the shear modulus μ, are given in Table 1.

These equations are solved using the Fourier transform in time t and in the horizontal direction x,

$$F(k, z, t) = \int_{-\infty}^{\infty} \int_{-\infty}^{\infty} f(x, z, t) \exp\left[i\left(kx - \omega t\right)\right] \mathrm{d}x\mathrm{d}t \tag{4}$$

This definition introduces the horizontal wavenumber k and frequency ω. Transform domain quantities are denoted with capital letters. Applying the transform of Equation 4 to the gov-

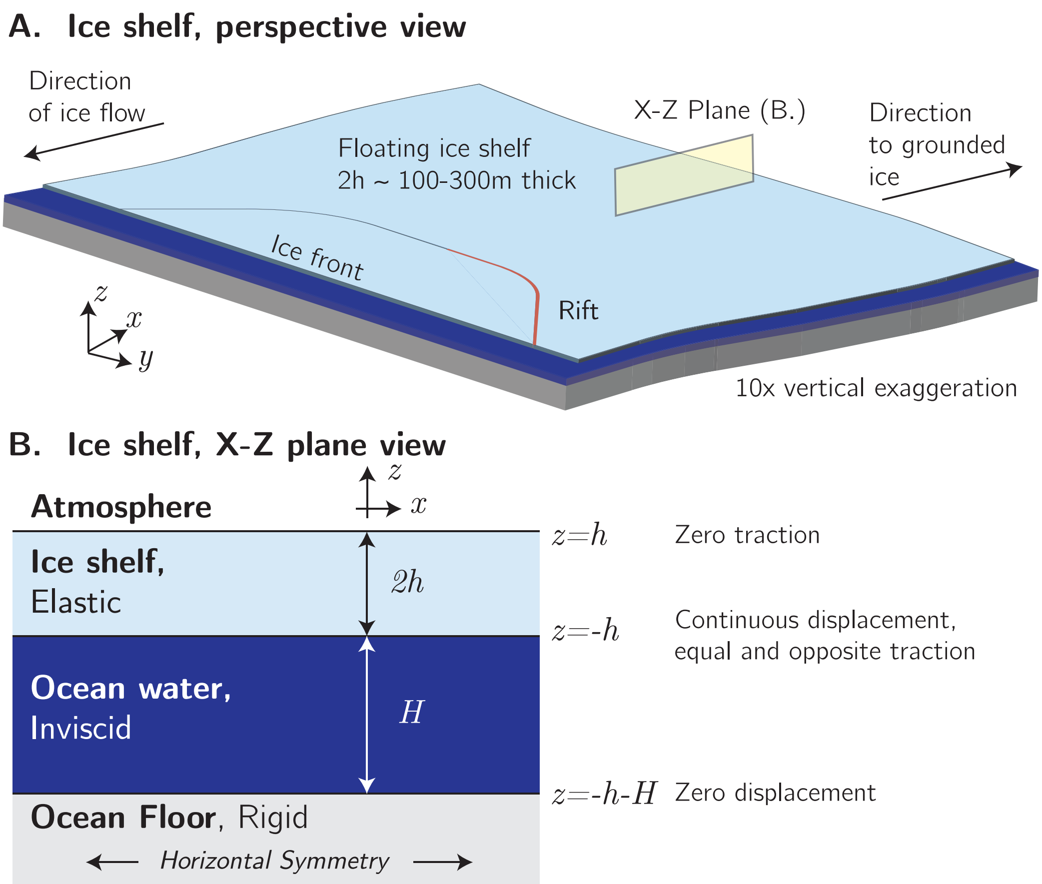

86 **Figure 1.** Model geometry showing the ice–atmosphere, ice–ocean, and ocean–solid earth boundaries.

erning equations (Equations 1-3) gives rise to a system of two coupled ordinary differential equations with derivatives in z. These equations have solution [*Graff*, 2012],

$$U_x = ik\,(A\sin\alpha z + B\cos\alpha z) + i\beta\,(C\cos\beta z - D\sin\beta z)\,, \tag{5}$$
$$U_z = \alpha\,(A\cos\alpha z - B\sin\alpha z) + k\,(C\sin\beta z + D\cos\beta z)\,, \tag{6}$$

where,

$$\alpha = k\sqrt{\left(\frac{\omega}{kc_p}\right)^2 - 1}, \tag{7}$$
$$\beta = k\sqrt{\left(\frac{\omega}{kc_s}\right)^2 - 1}. \tag{8}$$

The boundary conditions at the ice-atmosphere boundary $z = h$, are

$$\sigma_{xz}(h) = 0, \tag{9}$$
$$\sigma_{zz}(h) = 0. \tag{10}$$

Two other boundary conditions are required, and these occur at the ice–ocean interface.

2.2 Ice–ocean coupling

The unperturbed ice–ocean interface is located at $z = -h$. The ice–ocean boundary moves in response to perturbations, with the deformed interface located at

$$z = -h + \phi(x, t). \tag{11}$$

Consistent with a linearized theory of wave propagation, I assume that such geometric changes are small and following standard treatments [*Lipovsky and Dunham*, 2015; *Gill*, 2016] I prescribe boundary conditions on the undeformed interface. At this boundary, the force exerted on the ice by the water $\delta p(x, t)$ is equal and opposite to the force exerted by the water on the ice σ_{zz},

$$\sigma_{zz}(-h) = -\delta p(x, t). \tag{12}$$

The ocean is treated as invicid so there is no shear stress,

$$\sigma_{xz}(-h) = 0. \tag{13}$$

And by continuity the velocities must match between the fluid and solid,

$$\frac{\partial u_z}{\partial t}(-h) = v_z, \tag{14}$$

where v_z is the vertical fluid velocity. I next examine motions in the sub-ice ocean waters with the goal of describing the fields δp and v_z (Equations 12 and 14) on the ice–ocean interface.

2.3 Flow in the ocean cavity

I examine the behavior of perturbations to a sub-ice shelf cavity initially at rest. In this initial state, the pressure in the water is,

$$p_0(z) = \rho_w g(z + h) + \rho_i g(2h). \tag{15}$$

I then define the total fluid pressure p' to be

$$p'(x, z, t) = p(x, z, t) + p_0(z) \tag{16}$$

Shear modulus	μ	3.5 GPa
Lamé parameter	λ	6.8 GPa
Young's modulus	E	9.3 GPa
Poisson ratio	ν	0.33
	$\gamma^2 \equiv c_s/c_p$	0.52
Density of ice	ρ	916 kg/m^3
Density of seawater	ρ_w	1024 kg/m^3
Dilatational wave speed	c_p	3750 m/s
Shear wave speed	c_s	1950 m/s

Table 1. Table of ice mechanical properties [*Schulson et al.*, 2009].

Flow perturbations follow the linearized equations for an incompressible, inviscid flow with uniform density. The horizontal and vertical momentum balance equations are

$$\rho_w \frac{\partial v_x}{\partial t} = -\frac{\partial p}{\partial x} \tag{17}$$

$$\rho_w \frac{\partial v_z}{\partial t} = -\frac{\partial p}{\partial z}. \tag{18}$$

Here v_x and v_z are the x- and z-components of fluid velocity. The statement of mass conservation may be combined with Equations 17 and 18 with the result being Laplace's equation for pressure *Gill* [2016],

$$\nabla^2 p = 0. \tag{19}$$

The boundary condition at the ocean bottom, $z = -h - H$, is that vertical velocities vanish,

$$v_z(z = -h - H) = 0. \tag{20}$$

At the ice–ocean interface, the water pressure perturbation is equal to the hydrostatic pressure from the interface perturbation plus the pressure exerted by the ice on the water,

$$p(-h) = \rho_w g \phi(x,t) + \delta p(x,t). \tag{21}$$

The fluid equations (19-21) may be solved in the transform domain using Equation 4. The result is a transfer function between ΔP and surface height Φ,

$$\Delta P = \rho_w g \left(\frac{\omega^2}{gk} \coth(kH) - 1 \right) \Phi \equiv -T(k,\omega)\Phi. \tag{22}$$

This transfer function, combined with the the ice–ocean coupling conditions (Equations 12 and 14), allows me to write the entire coupled ice–ocean problem exclusively in terms of boundary conditions on the elastic solid. In Equation 22, ΔP and Φ can be eliminated in favor of the field variables Σ_{zz} and U_z, defined in the elastic solid. The result is the bottom boundary conditions on the elastic ice layer,

$$\Sigma_{zz}(z = -h) = T(k,\omega) U_z(z = -h), \tag{23}$$

$$\Sigma_{xz}(z = -h) = 0. \tag{24}$$

It is interesting to note that ice–ocean coupling manifests itself as the condition in Equation 23, namely, as a Robin type boundary condition that relates the vertical elastic displacement to the vertical compressive elastic stress.

2.4 The dispersion relation

The four boundary conditions (Equations 9, 10, 23, and 24) on the elastic solid result in a homogeneous system of equations,

$$\left\{\begin{bmatrix} 2\left(k^2-\beta^2\right)\mu\cos(h\alpha) & 4k\beta\mu\cos(h\beta) & 0 & 0 \\ 2k\alpha\sin(h\alpha) & \left(\beta^2-k^2\right)\sin(h\beta) & 0 & 0 \\ 0 & 0 & 4k\beta\mu\sin(h\beta) & 2\left(\beta^2-k^2\right)\mu\sin(h\alpha) \\ 0 & 0 & \left(k^2-\beta^2\right)\cos(h\beta) & 2k\alpha\cos(h\alpha) \end{bmatrix} - T\begin{bmatrix} \alpha\sin(h\alpha) & -k\sin(h\beta) & k\cos(h\beta) & \alpha\cos(h\alpha) \\ 0 & 0 & 0 & 0 \\ \alpha\sin(h\alpha) & -k\sin(h\beta) & k\cos(h\beta) & \alpha\cos(h\alpha) \\ 0 & 0 & 0 & 0 \end{bmatrix}\right\}\begin{pmatrix} B \\ C \\ D \\ A \end{pmatrix} = \begin{pmatrix} 0 \\ 0 \\ 0 \\ 0 \end{pmatrix} \quad (25)$$

Solutions to these equations require a vanishing determinant, and this condition gives rise to the dispersion relation,

$$D(k,\omega) = D_E(k,\omega)D_F(k,\omega) + D_{HD}(k,\omega) = 0. \quad (26)$$

where,

$$D_F \equiv \frac{\tan(\alpha h)}{\tan(\beta h)} + \frac{\left(k^2-\beta^2\right)^2}{4\alpha\beta k^2}, \quad (27)$$

$$D_E \equiv \frac{\tan(\alpha h)}{\tan(\beta h)} + \frac{4\alpha\beta k^2}{\left(k^2-\beta^2\right)^2}, \quad (28)$$

$$D_{HD} \equiv \frac{T}{2\mu}\frac{\alpha\left(\beta^2+k^2\right)\left[\tan^2(\alpha h)-1\right]}{4\alpha\beta k^2\tan(\beta h)}\left[\frac{\tan^2(\beta h)-1}{\tan^2(\alpha h)-1} + \frac{\tan(\alpha h)}{\tan(\beta h)}\frac{4\alpha\beta k^2}{\left(k^2-\beta^2\right)^2}\right]. \quad (29)$$

When ice–ocean coupling is absent, $T = 0$ and so $D_{HD} = 0$. In this case Equation 26 reduces to the Lamb wave dispersion relation. This dispersion relation corresponds to the motions of an elastic layer in a vacuum [*Graff*, 2012]. The Lamb wave dispersion relation is notable because it consists of uncoupled flexural and extensional modes. Mathematically this uncoupling occurs because it is possible to factor the dispersion relation into the product of two terms, D_E and D_F. Equation 26 is equivalent to Equation 49 of *Wang and Shen* [2010] in the case of a perfectly elastic ice layer.

In general, the mechanical interaction that occurs at the ice–ocean interface results in coupling between the flexural and extensional motions of the ice shelf. For this reason, there are no longer uncoupled flexural and extensional modes over the entire frequency- and wavenumber-spectra as there is in the more specific Lamb wave case. I will show in the next section, however, that for wavelengths that are long compared to the ice thickness, a simplification to extensional and flexural modes occurs.

3 The long wavelength limit

As I will discuss more in Section 5, seismic observations from Antarctic ice shelves motivate the study of waves with wavelength greater than the ice thickness. I therefore calculate the Taylor series in the small parameter kh for the dispersion relation of Equation 26,

$$D_F \approx \frac{1}{12}\left(\frac{\omega}{kc_s}\right)^2\left\{\frac{\omega^2}{c_s^2k^2}\left[2\left(\gamma^2-1\right)^2h^2k^2-3\right] + 4\left(\gamma^2-1\right)h^2k^2\right\}, \quad (30)$$

$$D_E \approx \frac{1}{4}\left(\frac{\omega}{kc_s}\right)^2\left[4\left(\gamma^2-1\right) + \left(2\gamma^4-1\right)\frac{\omega^2}{c_s^2k^2}\right], \quad (31)$$

$$D_{HD} \approx \frac{T}{8\mu hk^2}\frac{1}{4}\left(\frac{\omega}{kc_s}\right)^4\left[4\left(\gamma^2-1\right) + \left(2\gamma^4-1\right)\frac{\omega^2}{c_s^2k^2}\right]\left[\frac{\gamma^2+1}{2}\frac{\omega^2}{k^2c_s^2}+1\right]. \quad (32)$$

I have defined $\gamma \equiv \sqrt{c_s/c_p}$. The resulting expression for the dispersion relation permits factorization into the form,

$$D(k,\omega) \approx \left(\frac{\omega}{c_s k}\right)^4 \left\{4\left(\gamma^2-1\right)+\left(2\gamma^4-1\right)\left(\frac{\omega}{c_s k}\right)^2\right\} \times \left\{4\left(\gamma^2-1\right)h^2k^2+\frac{3T}{2h\mu k^2}\left[\frac{\gamma^2+1}{2}\left(\frac{\omega}{c_s k}\right)^2+1\right] + \left[2\left(\gamma^2-1\right)^2 h^2k^2-3\right]\left(\frac{\omega}{c_s k}\right)^2\right\}, \tag{33}$$

which has the property that it consists of two uncoupled modes.

3.1 Extensional mode

The first mode, corresponding to the first curly-bracketed term, is identical to the long wavelength symmetric Lamb wave mode. This mode has nondispersive phase velocity

$$\frac{\omega}{k} = \sqrt{\frac{E}{\rho_i(1-\nu^2)}}. \tag{34}$$

This phase velocity is the plane strain equivalent of the wave speed in a one-dimensional elastic bar, $\sqrt{E/\rho_i}$. For the material properties of ice (Table 1), this phase velocity is equal to 3375 m/s.

The extensional mode does not exhibit any ice–ocean interaction.

3.2 Flexural mode

The second mode, corresponding to the second curly-bracketed term, is a modification of the long wavelength antisymmetric Lamb wave mode. The dispersion relation for this mode is,

$$4\left(1-\gamma^2\right)h^2k^2+\frac{3}{2}\frac{T}{h\mu k^2}\left[\frac{\gamma^2+1}{2}\left(\frac{\omega}{c_s k}\right)^2+1\right]+\left[2\left(\gamma^2-1\right)^2h^2k^2-3\right]\left(\frac{\omega}{c_s k}\right)^2=0. \tag{35}$$

Keeping only the lowest order terms in the small parameter kh gives

$$Dk^4 - 2h\rho_i\omega^2 = -T, \tag{36}$$

where $D \equiv \frac{8}{3}\mu(1-\gamma^2)h^3$ is the flexural rigidity. I have not yet made use of the ice-ocean transfer function. The results in this section up to this point are therefore valid for any ice–ocean transfer function T.

3.3 Flexural gravity waves

Using the ice–ocean transfer function (Equation 22) results in the dispersion relation for flexural gravity waves,

$$\omega^2 = \frac{Dk^5/\rho_w + gk}{\coth(kH) + 2hk\rho_i/\rho_w}. \tag{37}$$

This dispersion relation was first derived by *Greenhill* [1886]. Noting that the right term in the denominator is order hk while the left term ranges between order 1 and order $1/(Hk)$ suggests that the former is small compared to the latter. This conclusion assumes that h and H are the same order of magnitude, a reasonable assumption for ice shelves. Physically this means that the inertia of the ice is less important than the inertia of the water. Dropping this term gives,

$$\omega^2 = gk\left[\left(\frac{\lambda_{fg}}{\lambda}\right)^4 + 1\right]\tanh(kH), \tag{38}$$

with flexural-gravity wave length,

$$\lambda_{fg} \equiv 2\pi\left(\frac{D}{g\rho_w}\right)^{1/4} \tag{39}$$

The flexural-gravity wave length λ_{fg} separates two regimes of wave behavior. When $\lambda > \lambda_{fg}$, the dispersion relation is $\omega^2 = gk\tanh(kH)$, which is the dispersion relation for surface gravity waves. In this limit the dominant restoring force is gravity; elasticity does not enter the dispersion relation. When $\lambda < \lambda_{fg}$, the dispersion relation is $\omega^2 = Dk^5\tanh(kH)/\rho_w$. In this limit the dominant restoring force is elasticity; gravity does not enter the dispersion relation. This transition between two wave types is illustrated in Figure 2, which plots the flexural gravity wave phase velocity as a function of frequency for a particular geometry relevant to the Ross Ice Shelf.

4 Stresses and particle motions of ice shelf waves

In order to analyze seismograms recorded on ice shelves, I now calculate the stresses and particle motions associated with long period flexural and extensional waves. First, in order to infer stress changes from velocity seismograms, I calculate the transfer function between these two quantities. This transfer function is called the wave impedance,

$$Z_{ijk}(k,\omega) = \frac{\Sigma_{ij}(k,\omega)}{(-i\omega)U_k(k,\omega)}. \tag{40}$$

Impedance has previously been treated as a tensorial quantity in the context of surface waves in anisotropic media [*Barnett and Lothe*, 1985]. As evidenced by the general dependence on wavenumber k and frequency ω, dispersive waves may have wavenumber- k and frequency-ω dependent impedance tensor components.

The impedance tensor defined in this way allows the estimation of wave field stresses using multiplication in the Fourier domain,

$$\sigma_{ij}(x,t) = \int_{-\infty}^{\infty}\int_{-\infty}^{\infty} Z_{ijk}(k,\omega)U_k(k,\omega)e^{i(kx-\omega t)}\mathrm{d}k\mathrm{d}\omega. \tag{41}$$

In the following I derive wave impedances for long period flexural and extensional waves. This integration is revisited in Equation 54.

I calculate particle motions by regrouping the general solution (Equations 5 and 6) into symmetric and antisymmetric terms. These terms correspond to extensional and flexural motions, respectively,

$$\frac{U_x^F}{A} = ik\sin\alpha z - i\frac{D}{A}\beta\sin\beta z, \tag{42}$$

$$\frac{U_z^F}{A} = \alpha\cos\alpha z + \frac{D}{A}k\cos\beta z, \tag{43}$$

$$\frac{U_x^E}{C} = i\frac{B}{C}k\cos\alpha z + i\beta\cos\beta z, \tag{44}$$

$$\frac{U_z^E}{C} = -\frac{B}{C}\alpha\sin\alpha z + k\sin\beta z. \tag{45}$$

The ratios D/A and B/C are defined from the zero shear stress boundary conditions at $z = \pm h$, as expressed in the second and fourth lines of the matrix in Equation 25,

$$\frac{B}{C} = \frac{(k^2 - \beta^2)\sin(h\beta)}{2k\alpha\sin(h\alpha)} \tag{46}$$

$$\frac{D}{A} = \frac{2k\alpha\cos(h\alpha)}{(\beta^2 - k^2)\cos(h\beta)} \tag{47}$$

The other boundary conditions enter through the requirement that k and ω be related by the dispersion relation. The equations for particle motion (Equations 42-47), combined with the elastic constitutive relation (Equation 3), suffice to calculate the impedance tensor of Equation 40.

4.1 Extensional mode

In the long wavelength limit, $B/C \approx D/A \approx -i$. Extensional motions have particle motions,

$$\frac{U_x^E}{C} \approx -2k, \tag{48}$$

$$\frac{U_z^E}{C} \approx 2i(kz)k. \tag{49}$$

I note that the long wavelength limit $kh \ll 1$ is distinct from the quasi static limit where $\omega/(kc_p) \ll 1$. In other words, long wavelength extensional waves are not quasi static. The long wavelength extensional mode has dominantly horizontal displacements $|U_x^E|/|U_z^E| \sim (kz)^{-1}$ that are constant throughout the ice layer. The much smaller vertical displacements, in contrast, are antisymmetric about the midplane of the ice layer.

The extensional mode has σ_{xx}-to-u_x impedance component,

$$Z_{xxx}^E = -\frac{\lambda\frac{\partial U_z}{\partial z}}{-i\omega U_x} - \frac{ik(\lambda+2\mu)U_x}{-i\omega U_x} \approx -\frac{2\mu}{\omega/k}. \tag{50}$$

I recall from Equation 34 that the extensional mode has constant ω/k. For the material properties of ice $Z_{xxx}^E \approx 2.07$ kPa/(mm/s). This value is greater than the s-wave impedance by a factor of two yet smaller than the p-wave impedance by about 50%.

I have chosen to focus on the Z_{xxx}^E impedance tensor component because it relates the largest extensional displacement u_x to the horizontal compressive stress σ_{xx}. The horizontal compressive stress σ_{xx} is of interest to the process of rift propagation, as discussed in a forthcoming companion paper.

4.2 Flexural mode

In the long wavelength limit, flexural motions have phase velocity given by Equation 38. The particle motions satisfy,

$$\frac{U_x^F}{A} \approx -\frac{k^2\omega^2 z}{2\gamma^2} \tag{51}$$

$$\frac{U_z^F}{A} \approx -\frac{ik\omega^2}{2\gamma^2} \tag{52}$$

Unlike the extensional mode, the flexural mode long wavelength limit is also quasi static. The long wavelength flexural mode has dominantly vertical displacements $|U_z^F|/|U_x^F| \sim (kz)^{-1}$ that are constant throughout the ice layer. The much smaller horizontal displacements, in contrast, are antisymmetric about the midplane of the ice layer.

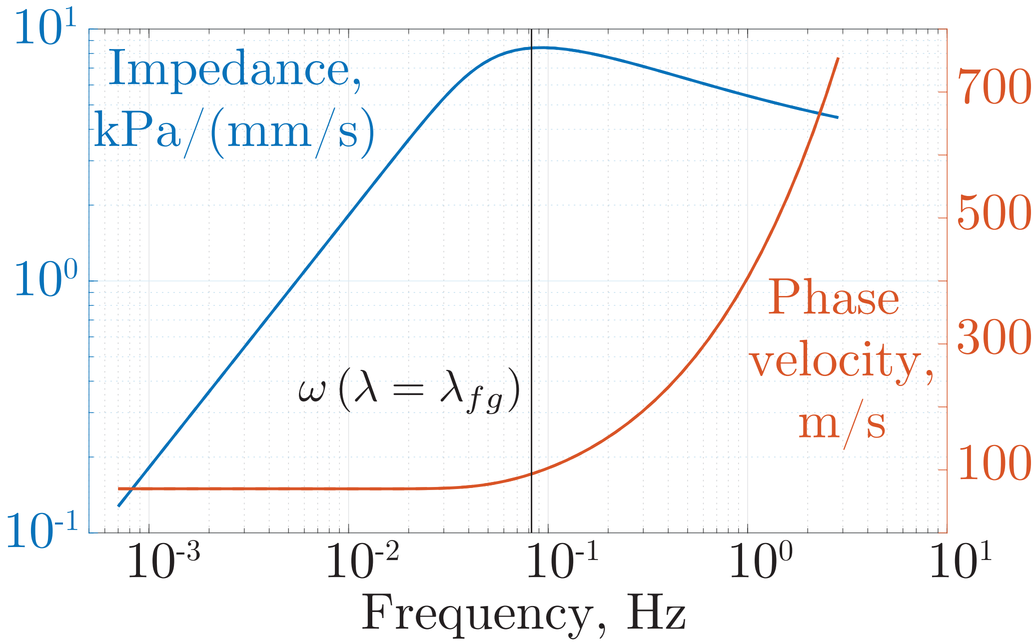

Figure 2. Wave speed and impedance of flexural gravity waves. Curves are calculated for water depth H = 483 and ice thickness $2h = 265$ m. Both curves are drawn until $2hk = 1$.

The flexural mode has σ_{xx}-to-u_z impedance component,

$$Z^F_{xxz} \approx -ikz\frac{4\mu\left(1-\gamma^2\right)}{\omega/k} \tag{53}$$

This result shows that the stresses carried by an antisymmetric ice shelf wave are a function of the properties of the ocean waters. I have chosen to focus on the xxz component of the impedance tensor for the same reasons as discussed in the previous section. The expression in Equation 53 agrees with the result derived from beam theory, for example using Equation 36 in *Sergienko* [2017].

Figure 2 plots flexural mode impedance. Impedance reaches a maximum at the frequency associated with the flexural-gravity wavelength λ_{fg}. Below this frequency, impedance increases proportional to frequency ω. Above this frequency, impedance is a decreasing function of frequency. At $\omega = 0.1$ Hz, and for a 265 ice thickness at 483m water depth as is approximately true of the Ross Ice Shelf, $Z^F_{xxz} \approx 8.5$ kPa/(mm/s).

Flexural stresses may be systematically estimated from a vertical component velocity seismogram $v(t) = \partial u_z/\partial t$ by convolving a velocity time series with the transfer function in Equation 53,

$$\sigma_{xx}(z = h, t) = \mu' z \int \frac{-i\omega V(\omega)}{\left[c\,(\omega)\right]^2} e^{i\omega t}\, \mathrm{d}\omega. \tag{54}$$

In this expression, $\mu' = 4\mu\left(1-\gamma^2\right)$ and I have used the definition of the phase velocity as $c \equiv \omega/k$ to eliminate reference to the wavenumber k. A simplified case occurs for wavelengths longer than the water depth H and the flexural-buoyancy wavelength λ_{fg}. In this case $c^2 = gH$ is nondispersive and therefore independent of frequency. The integral in Equation 54 may therefore be evaluated as

$$\sigma_{xx}(z, t) = \frac{\mu' z}{gH}\frac{\partial V}{\partial t}. \tag{55}$$

This result is interesting because it shows that flexural gravity waves have stresses that are proportional to particle acceleration. This is in contrast to body waves which have stresses that are proportional to particle velocity.

5 Analysis of observations from the Ross Ice Shelf, Antarctica

I analyze continuously recorded seismograms from seismometers on the Ross Ice Shelf, Antarctica (Figure 4). This data has been previously described by *MacAyeal et al.* [2006] and *Cathles et al.* [2009]. I examine data from the station RIS2, temporary network code XV, during the 2005-2006 deployment [*Okal and MacAyeal*]. The station RIS2 is particularly useful because it was located near the tip of a ~ 40 km long rift in the Ross Ice Shelf. This rift will one day connect to the ice front and form a large tabular iceberg. The block that will become this iceberg is still attached and has been called the Nascent Iceberg by *MacAyeal et al.* [2006]. The station was located on ice with thickness 265 m above a sub shelf cavity with water depth 483 m.

I obtain seismograms from the IRIS consortium website. I first taper and then bandpass filter all raw seismic traces. The bandpass filter has cutoff frequencies 0.0001, 0.0002, 0.2, and 0.4 Hz. I then remove the instrumental response from all seismograms. Because signals of interest may have frequency content near or below the nominal instrumental sensitivity, this is a critical step in the data processing in order to ensure that the relative amplitudes of signals with varying frequency content are accurately quantified. In all of my analysis I focus on the LH channels that are sampled at 1 Hz. There is 167 d of data with one data outage of several days in late March 2006.

The waveforms recorded at RIS2 are shown in the spectrogram in Figure 3. The principal feature in the spectrogram is the arrival of ocean swell from distant storms. These waves appear as upward sloping spectral lines. This occurs because long period ocean swell travels faster and therefore arrives before short period swell. This signal has been described extensively by *MacAyeal et al.* [2006] and *Cathles et al.* [2009] and the interested reader is referred there for more details. The principal goal here is to describe the stress changes associated with these waves.

5.1 Flexural stresses

The flexural-gravity length at the RIS2 site is $\lambda_{fg} = 10.4$ km (Equation 39). Using the flexural gravity wave dispersion relation (Equation 38), I calculate that this wavelength corresponds to a wave frequency of 0.04 Hz. At this site on the Ross Ice Shelf, waves with frequency greater than 0.04 Hz are therefore expected to have restoring force from elasticity, and waves with lower frequency are expected to have restoring force due to gravity. The long wavelength limit, which occurs for waves with wavelength greater than $\lambda \sim h$, corresponds to a wave period of 1.0 s.

Figure 4a shows a 30 minute seismogram that was recorded during the arrival of ocean surface gravity waves from a distant storm [*Cathles et al.*, 2009]. This seismogram is high pass filtered above 100s. Wave energy in this seismogram is concentrated broadly around 0.06 Hz. This frequency is near the frequency associated with the flexural-buoyancy wavelength as calculated in the previous paragraph. This suggests that waves in the dominant frequency band experience a combination of restoring forces due to both gravity and elasticity.

The stresses associated with flexural gravity waves on the Ross Ice Shelf are shown in Figure 5. There was a cumulative total of ~ 1000 s during the observation period with wave induced stresses with greater than 1 kPa amplitude. Stresses were inferred using Equation 54. Flexural gravity wave impedance is maximal near the frequency associated with the flexural gravity wavelength (Figure 2). Because the station RIS2 also happens to have elevated wave activity in this frequency range, the resulting stresses are relatively large.

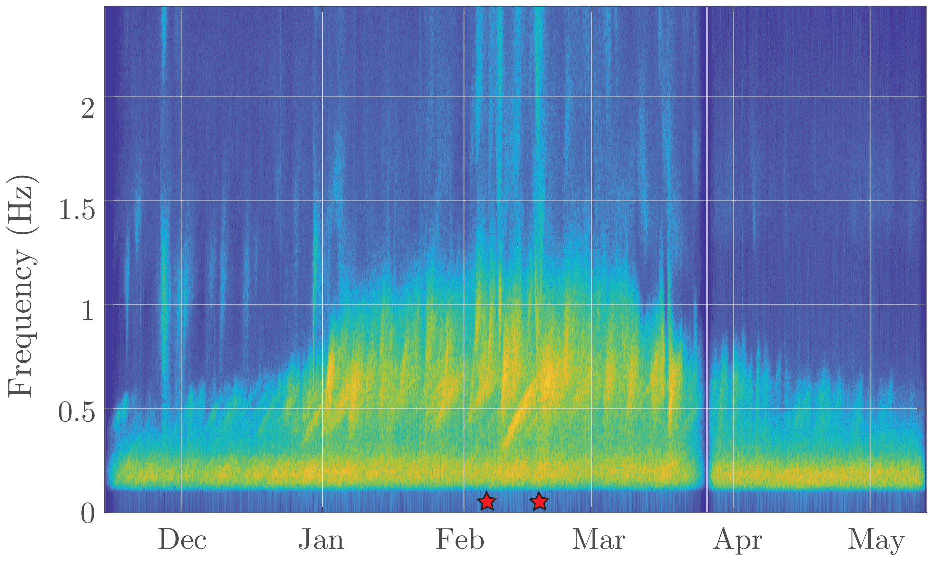

Figure 3. Spectrogram of the data from the RIS2 site. Upward sloping spectral bands show the arrival of ocean swell from distant storms. The red stars mark the time periods shown in Figure 4.

5.2 Extensional stresses

The same seismic network operating on the Ross records dominantly horizontal motions at lower frequencies. With ice thickness 265 m the long-wavelength limit $kh \ll 1$ corresponds to symmetric waves with frequency $(3375 \text{ m/s})/(4\pi h) \approx 1$ Hz. A seismogram is shown in Figure 4b from RIS2, this time bandpass filtered between 1000 and 100 s. Horizontal motions have the largest amplitude in this frequency range, as is typical of the long wavelength symmetric Lamb wave (Equations 48 and 49). Using the estimate of the extensional mode impedance from Equation 50 results in an estimate of the stress change carried by this wave as being $\sigma_{xx} \approx 0.6 \text{ mm/s} \times 2.07 \text{ kPa/(mm/s)} \approx 1.24$ kPa.

6 Conclusions

I have described coupled ice–ocean wave propagation in floating ice shelves. Although the resulting analysis, i.e., the dispersion relation of Equation 26, is applicable over a wide range of frequencies and wavelengths, I have placed particular emphasis on the behavior of waves with wavelengths longer than the ice thickness. Wave motion in the long wavelength limit occurs as either flexural or extensional modes (Equation 33). Of these modes, only the flexural mode exhibits ice–ocean coupling in the long wavelength limit. This coupling is manifest in the simplified dispersion relation, Equation 36, which can be written in a form applicable for arbitrary ice–ocean transfer function $T(k, \omega)$.

I have demonstrated how to use this theory to infer the stresses associated with a seismically observed wave field. I have applied this method to data from the Ross Ice Shelf, where I conclude that the vertical motions associated with long period flexural gravity waves create larger stress changes than the longer-period extensional motions, despite the fact that the extensional motions have higher particle velocity amplitudes.

The largest inferred stress had amplitude 2.3 kPa and was due to long period flexural waves. Because the flexural stresses vary linearly throughout the ice thickness, this flexural

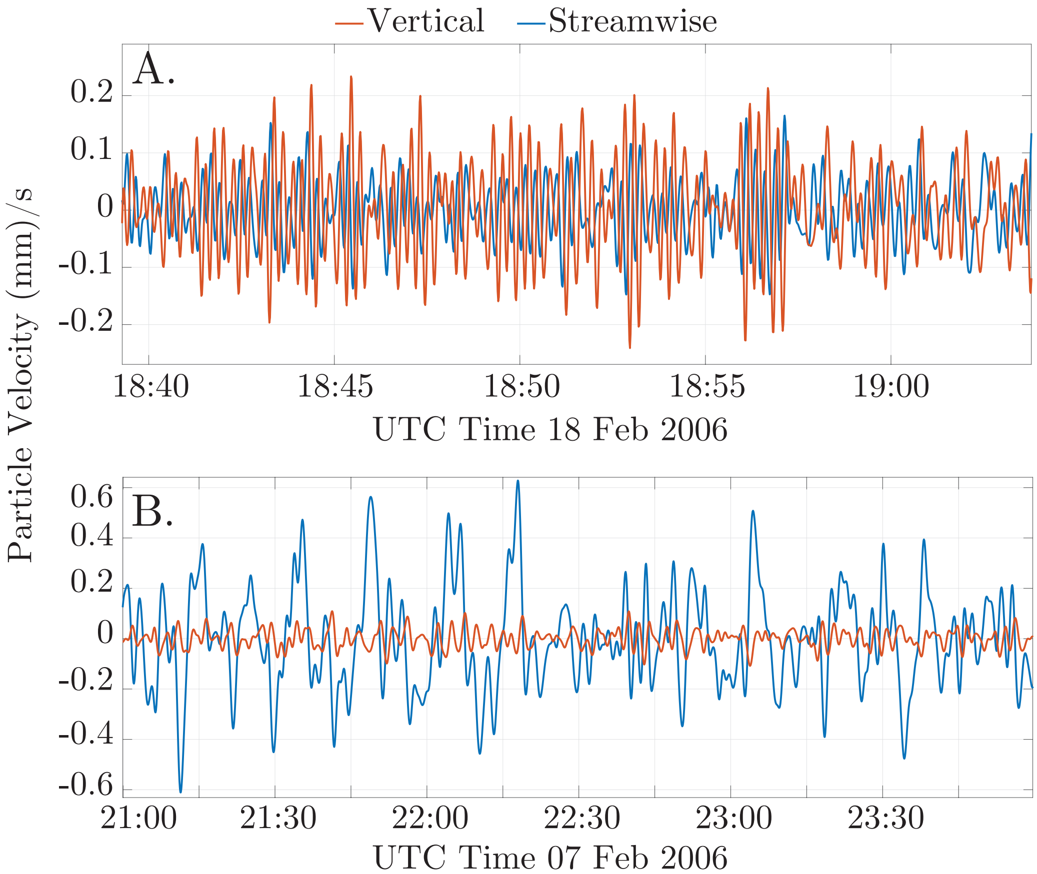

Figure 4. Seismograms from the Ross Ice Shelf recorded during periods of elevated wave activity. Note the different horizontal and vertical axes. A. Seismogram showing equal horizontal and vertical components of velocity recorded during the arrival of waves from a distant storm [*Cathles et al.*, 2009]. B. Seismogram recorded at the same site during a time with elevated horizontal motion.

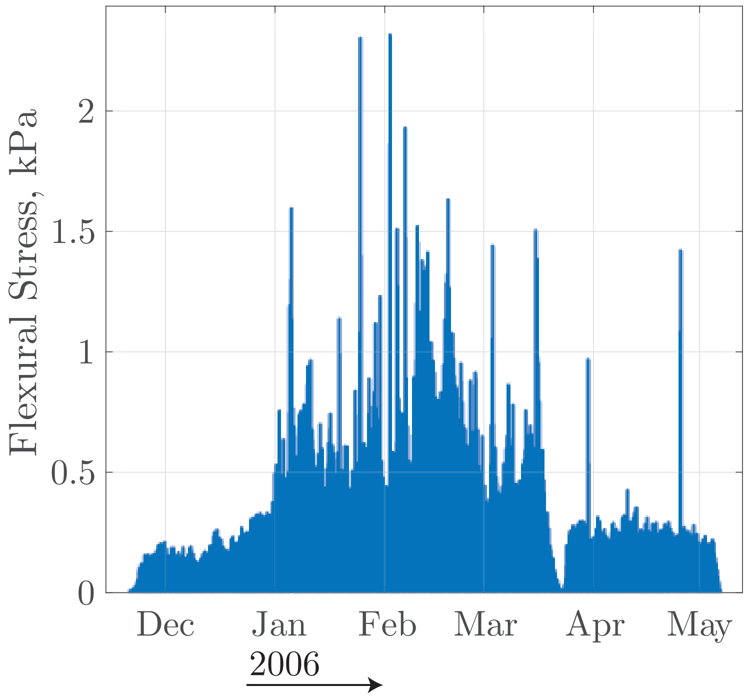

Figure 5. A. Calculated stresses carried by flexural waves using Equation 54. The highest stresses occur during the arrival of waves from distant storms in Jan-Mar 2006.

stress creates a net moment on the ice shelf [*Reeh*, 1968]

$$M = \int_{-h}^{h} \sigma_{xx}(z) z \mathrm{d}z = \frac{\sigma_{xx}^{\max}}{h} \int_{-h}^{h} z^2 \mathrm{d}z = \frac{(2h)^2}{6} \sigma_{xx}^{\max}, \tag{56}$$

which gives a net moment $M \approx 26$ MNm. For comparison, the net moment generated by the difference in hydrostatic pressure at the vertical cliff face of the calving front is approximately 450 times larger than this value [*Reeh*, 1968]. This calculation verifies that ocean waves are indeed small perturbations acting on the ice shelf–ocean system.

Additional applications of the theory developed here are possible. The description of elastic-gravity wave propagation is applicable to wave propagation in planetary ice shells, albeit only over distances sufficiently short that planetary curvature can be neglected. Current models of wave propagation on Europa, for example, do not generally incorporate the effect of flowing ocean waters beneath the ice layer [*Cammarano et al.*, 2006], as in earlier ice shelf studies [*Press and Ewing*, 1951]. The general theory of elastic-gravity waves, i.e. at wavelengths short compared to the ice shelf thickness, could also be used to analyze ice shelf normal modes [*Holdsworth and Glynn*, 1978; *Sergienko*, 2013]. These modes are expected to be dispersive and therefore have nontrivial overtone structure [*Graff*, 2012; *Lipovsky and Dunham*, 2015]. Future work could examine additional sources of excitation including tectonic earthquakes [*Baker et al.*, 2016] and ice stream stick slip [*Wiens et al.*, 2015; *Lipovsky and Dunham*, 2017]. In a forthcoming companion paper, the stresses inferred in the present work are compared to the stresses required to drive ice shelf rift propagation.

Acknowledgments
This work was supported by a Postdoctoral Fellowship in the Department of Earth and Planetary Sciences at Harvard University. Greg Wagner and Marine Denolle read earlier versions

of this paper and provided feedback. All of the data used in this study have been previously published and are freely available at the IRIS Consortium website [*Okal and MacAyeal*].

References

Baker, M. G., R. C. Aster, R. E. Anthony, D. Wiens, A. Nyblade, P. D. Bromirski, R. A. Stephen, and P. Gerstoft (2016), Chacterization of Teleseismic Earthquakes Observed on an Ice Shelf, *AGU Fall Meeting Abstracts*.

Banwell, A. F., I. C. Willis, G. J. Macdonald, B. Goodsell, D. P. Mayer, A. Powell, and D. R. Macayeal (2017), Calving and rifting on the mcmurdo ice shelf, antarctica, *Annals of Glaciology*, pp. 1–10.

Barnett, D., and J. Lothe (1985), Free surface (rayleigh) waves in anisotropic elastic half-spaces: the surface impedance method, in *Proceedings of the Royal Society of London A: Mathematical, Physical and Engineering Sciences*, vol. 402, pp. 135–152, The Royal Society.

Bartholomaus, T. C., C. F. Larsen, and S. O?Neel (2013), Does calving matter? evidence for significant submarine melt, *Earth and Planetary Science Letters*, *380*, 21–30.

Benn, D. I., C. R. Warren, and R. H. Mottram (2007), Calving processes and the dynamics of calving glaciers, *Earth-Science Reviews*, *82*(3), 143–179.

Bromirski, P., Z. Chen, R. Stephen, P. Gerstoft, D. Arcas, A. Diez, R. Aster, D. Wiens, and A. Nyblade (2017), Tsunami and infragravity waves impacting antarctic ice shelves, *Journal of Geophysical Research: Oceans*.

Bromirski, P. D., O. V. Sergienko, and D. R. MacAyeal (2010), Transoceanic infragravity waves impacting antarctic ice shelves, *Geophysical Research Letters*, *37*(2).

Bromirski, P. D., A. Diez, P. Gerstoft, R. A. Stephen, T. Bolmer, D. A. Wiens, R. C. Aster, and A. Nyblade (2015), Ross ice shelf vibrations, *Geophysical Research Letters*, *42*(18), 7589–7597.

Brunt, K. M., E. A. Okal, and D. R. MacAYEAL (2011), Antarctic ice-shelf calving triggered by the honshu (japan) earthquake and tsunami, march 2011, *Journal of Glaciology*, *57*(205), 785–788.

Cammarano, F., V. Lekic, M. Manga, M. Panning, and B. Romanowicz (2006), Long-period seismology on europa: 1. physically consistent interior models, *Journal of Geophysical Research: Planets*, *111*(E12).

Cathles, L., E. A. Okal, and D. R. MacAyeal (2009), Seismic observations of sea swell on the floating ross ice shelf, antarctica, *Journal of Geophysical Research: Earth Surface*, *114*(F2).

DeConto, R. M., and D. Pollard (2016), Contribution of antarctica to past and future sea-level rise, *Nature*, *531*(7596), 591–597.

Fricker, H., N. Young, R. Coleman, J. Bassis, and J.-B. Minster (2005), Multi-year monitoring of rift propagation on the amery ice shelf, east antarctica, *Geophysical Research Letters*, *32*(2).

Gill, A. E. (2016), *AtmosphereâĂŤocean dynamics*, Elsevier.

Golledge, N. R., D. E. Kowalewski, T. R. Naish, R. H. Levy, C. J. Fogwill, and E. G. Gasson (2015), The multi-millennial antarctic commitment to future sea-level rise, *Nature*, *526*(7573), 421.

Goodman, D., P. Wadhams, and V. Squire (1980), The flexural response of a tabular ice island to ocean swell, *Annals of Glaciology*, *1*(1), 23–27.

Graff, K. F. (2012), *Wave motion in elastic solids*, Courier Corporation.

Greenhill, A.-G. (1886), Wave motion in hydrodynamics, *American Journal of Mathematics*, pp. 62–96.

Holdsworth, G., and J. Glynn (1978), Iceberg calving from floating glaciers by a vibrating mechanism, *Nature*, *274*(5670), 464–466.

Hulbe, C. L., D. R. MacAyeal, G. H. Denton, J. Kleman, and T. V. Lowell (2004), Catastrophic ice shelf breakup as the source of heinrich event icebergs, *Paleoceanography*, *19*(1).

Konovalov, Y. (2014), Ice-shelf resonance deflections modelled with a 2-d elastic centre-line model, *Phys. Rev. Res. Int*, *4*, 9–29.

Lamb, H. (1917), On waves in an elastic plate, in *Proceedings of the Royal Society of London A: Mathematical, Physical and Engineering Sciences*, vol. 93, pp. 114–128, The Royal Society.

Lescarmontier, L., B. Legrésy, R. Coleman, F. Perosanz, C. Mayet, and L. Testut (2012), Vibrations of mertz glacier ice tongue, east antarctica, *Journal of Glaciology*, *58*(210), 665–676.

Lipovsky, B. P., and E. M. Dunham (2015), Vibrational modes of hydraulic fractures: Inference of fracture geometry from resonant frequencies and attenuation, *Journal of Geophysical Research: Solid Earth*, *120*(2), 1080–1107.

Lipovsky, B. P., and E. M. Dunham (2017), Slow-slip events on the whillans ice plain, antarctica, described using rate-and-state friction as an ice stream sliding law, *Journal of Geophysical Research: Earth Surface*, *122*(4), 973–1003.

MacAyeal, D. R., E. A. Okal, R. C. Aster, J. N. Bassis, K. M. Brunt, L. M. Cathles, R. Drucker, H. A. Fricker, Y.-J. Kim, S. Martin, et al. (2006), Transoceanic wave propagation links iceberg calving margins of antarctica with storms in tropics and northern hemisphere, *Geophysical Research Letters*, *33*(17).

Malvern, L. E. (1969), *Introduction to the Mechanics of a Continuous Medium*, Monograph.

Okal, E., and y. t. p. n. . O. d. S. MacAyeal, D ().

Press, F., and M. Ewing (1951), Propagation of elastic waves in a floating ice sheet, *Eos, Transactions American Geophysical Union*, *32*(5), 673–678.

Reeh, N. (1968), On the calving of ice from floating glaciers and ice shelves, *Journal of Glaciology*, *7*(50), 215–232.

Schoof, C., A. D. Davis, and T. V. Popa (2017), Boundary layer models for calving marine outlet glaciers, *The Cryosphere Discussions*, *2017*, 1–30, doi:10.5194/tc-2017-42.

Schulson, E. M., P. Duval, et al. (2009), *Creep and fracture of ice*, vol. 1, Cambridge University Press Cambridge.

Sergienko, O. (2010), Elastic response of floating glacier ice to impact of long-period ocean waves, *Journal of Geophysical Research: Earth Surface*, *115*(F4).

Sergienko, O. (2017), Behavior of flexural gravity waves on ice shelves: Application to the ross ice shelf, *Journal of Geophysical Research: Oceans*.

Sergienko, O. V. (2013), Normal modes of a coupled ice-shelf/sub-ice-shelf cavity system, *Journal of Glaciology*, *59*(213), 76–80.

Squire, V. A., J. P. Dugan, P. Wadhams, P. J. Rottier, and A. K. Liu (1995), Of ocean waves and sea ice, *Annual Review of Fluid Mechanics*, *27*(1), 115–168.

Walker, C., J. Bassis, H. Fricker, and R. Czerwinski (2013), Structural and environmental controls on antarctic ice shelf rift propagation inferred from satellite monitoring, *Journal of Geophysical Research: Earth Surface*, *118*(4), 2354–2364.

Wang, R., and H. H. Shen (2010), Gravity waves propagating into an ice-covered ocean: A viscoelastic model, *Journal of Geophysical Research: Oceans*, *115*(C6).

Wiens, D., M. J. Pratt, R. C. Aster, A. Nyblade, P. D. Bromirski, R. A. Stephen, P. Gerstoft, A. Diez, C. Cai, R. E. Anthony, and P. Shore (2015), Seismic Excitation of the Ross Ice Shelf by Whillans Ice Stream Stick-Slip Events, *AGU Fall Meeting Abstracts*.